

Understanding the Rocksalt-to-Wurtzite phase transformation through microstructural analysis of (Al,Sc)N epitaxial thin films

Bivas Saha, Sammy Saber, Eric A. Stach, Eric P. Kvam, and Timothy D. Sands

Citation: [Applied Physics Letters](#) **109**, 172102 (2016); doi: 10.1063/1.4966278

View online: <http://dx.doi.org/10.1063/1.4966278>

View Table of Contents: <http://scitation.aip.org/content/aip/journal/apl/109/17?ver=pdfcov>

Published by the [AIP Publishing](#)

Articles you may be interested in

[Enhanced hardness in epitaxial TiAlScN alloy thin films and rocksalt TiN/\(Al,Sc\)N superlattices](#)

Appl. Phys. Lett. **105**, 151904 (2014); 10.1063/1.4898067

[High performance AlScN thin film based surface acoustic wave devices with large electromechanical coupling coefficient](#)

Appl. Phys. Lett. **105**, 133502 (2014); 10.1063/1.4896853

[Microstructure and ferroelectric properties of epitaxial cation ordered PbSc_{0.5}Ta_{0.5}O₃ thin films grown on electroded and buffered Si\(100\)](#)

J. Appl. Phys. **114**, 084107 (2013); 10.1063/1.4819384

[Atomic layer deposition of Sc₂O₃ for passivating AlGaIn/GaN high electron mobility transistor devices](#)

Appl. Phys. Lett. **101**, 232109 (2012); 10.1063/1.4770071

[Microstructure and dielectric properties of piezoelectric magnetron sputtered w-Sc_xAl_{1-x}N thin films](#)

J. Appl. Phys. **111**, 093527 (2012); 10.1063/1.4714220

The image shows the cover of an Applied Physics Reviews journal. It features a blue and orange color scheme with a molecular structure background. The text 'NEW Special Topic Sections' is prominently displayed in white. Below it, 'NOW ONLINE' is written in yellow, followed by the title 'Lithium Niobate Properties and Applications: Reviews of Emerging Trends' in white. The AIP Applied Physics Reviews logo is in the bottom right corner.

NEW Special Topic Sections

NOW ONLINE
Lithium Niobate Properties and Applications:
Reviews of Emerging Trends

AIP Applied Physics
Reviews

Understanding the Rocksalt-to-Wurtzite phase transformation through microstructural analysis of (Al,Sc)N epitaxial thin films

Bivas Saha,^{1,a)} Sammy Saber,^{2,3} Eric A. Stach,⁴ Eric P. Kvam,^{2,3} and Timothy D. Sands⁵

¹Department of Materials Science and Engineering, University of California, Berkeley, California 94720, USA

²School of Materials Engineering, Purdue University, West Lafayette, Indiana 47907, USA

³Birck Nanotechnology Center, Purdue University, West Lafayette, Indiana 47907, USA

⁴Center for Functional Nanomaterials, Brookhaven National Laboratory, Upton, New York 11973-5000, USA

⁵Bradley Department of Electrical and Computer Engineering and Department of Materials Science and Engineering, Virginia Tech, Blacksburg, Virginia 24061, USA

(Received 25 August 2016; accepted 12 October 2016; published online 26 October 2016)

Rocksalt-to-wurtzite structural phase transitions in semiconducting materials (such as III–V nitrides, ZnO, CdSe, and others) have been studied for several decades. Almost all experimental works related to this phase transition involve diamond anvil cells to apply hydrostatic pressure, and as a result, direct observation of the microstructural transformation during the phase transition has not been possible. In this article, we have addressed and uncovered the intimate microstructural details and epitaxial relationships between phases by capturing what is essentially a thin-film snapshot of the transformation after growth of $\text{Al}_x\text{Sc}_{1-x}\text{N}$ films with a composition chosen to be close to the equilibrium phase boundary between wurtzite and rocksalt. The results support the hypothesis that the transformation is triggered by defects at $rs\text{-}\{011\}$ growth fronts that offer a nearly invariant plane with respect to the parallel $w\text{-}\{2\bar{1}10\}$ planes. The intermediate crystal structures and their epitaxial relationships are consistent with theoretical models that predict a transformation pathway involving homogeneous orthorhombic shear strain. *Published by AIP Publishing.*

[<http://dx.doi.org/10.1063/1.4966278>]

Epitaxial rocksalt metal/semiconductor superlattices based on transition metal nitrides (TMN) such as TiN/(Al,Sc)N have emerged as promising candidates for high temperature thermoelectric materials,^{1–4} plasmonic and hyperbolic metamaterials,^{5,6} and optoelectronic devices⁷ for solid state energy conversion. Since the constituent nitride materials are hard, corrosion resistant, mechanically and chemically stable, and exhibit extremely high melting temperatures (in excess of 3000 °C), they could find application in emitters and absorbers for thermophotovoltaics (STPV), the antenna head materials for heat assisted magnetic recording (HAMR), and high temperature transistors for harsh environment applications.^{8–10} For each such application, it is extremely important that the superlattices are structurally and morphologically stable at elevated operating temperatures (500 to >1000 °C) for extended periods of time.

While most TMNs (such as TiN, ZrN, HfN) adopt the cubic rocksalt crystal structure, the ubiquitous nitride semiconductors such as AlN, GaN, and InN crystallize in the wurtzite phase under ambient conditions.^{11,12} Previously, we have developed¹³ rocksalt $\text{Al}_x\text{Sc}_{1-x}\text{N}$ alloys by alloying AlN and semiconducting rocksalt ScN to lattice match with rocksalt TiN. The $\text{Al}_x\text{Sc}_{1-x}\text{N}$ alloy thin films are stable in the rocksalt phase with large critical thicknesses and with high AlN mole fractions.¹³ The TiN/ $\text{Al}_{0.72}\text{Sc}_{0.28}\text{N}$ metal/semiconductor superlattices developed on MgO substrates are the first demonstrations of epitaxial single crystalline metal/semiconductor superlattices^{3,5} with sharp interfaces and low densities of extended defects. Although much work

remains to control the electrical properties of these alloy semiconductors and their interfaces with metallic nitrides, the structural quality of these superlattices opens up the opportunity to develop a generation of artificially structured materials and devices.

Previous high-temperature stability analyses¹⁴ of epitaxial TiN/ $\text{Al}_x\text{Sc}_{1-x}\text{N}$ superlattices suggested that the metastable rocksalt $\text{Al}_{0.72}\text{Sc}_{0.28}\text{N}$ film undergoes a rocksalt to stable-wurtzite structural phase transition at 950 °C during annealing treatments lasting 120 h or more. Because of a 24% volume change associated with the transition, the structural integrity of the films and superlattices is severely compromised.¹⁵

The wurtzite-to-rocksalt phase transition is quite common in III–V nitride semiconductors (such as AlN, GaN, and InN) under extreme hydrostatic pressure. There have been studies since the early 1990s by various researchers to understand the details about such phase transitions.^{16–18} The B4 (wurtzite) to B1 (rocksalt) phase transitions are also observed in copper and silver halides^{19,20} and in more ionic materials such as ZnO.^{21,22} Several studies involving in-situ synchrotron X-ray diffraction (XRD) analysis²³ and in-situ Raman spectroscopy^{24,25} have been employed to understand the pressure dependence of such transitions, and first-principles calculations^{26,27} have also been performed to determine and understand the underlying mechanism. In spite of all such efforts, controversies about the exact mechanism of the transformation still persist, and modeling analyses often contradict experimental observations.²⁶ In-situ observation of the microstructural evolution from B4 to the B1 phase or vice versa is not feasible even with the most advanced state-of-the-art high-resolution transmission

^{a)}Author to whom correspondence should be addressed. Electronic mail: bsaha@berkeley.edu

electron microscopy (HRTEM), as the phase transition experiments are mostly performed inside a diamond anvil cell to apply high pressure. Moreover, the free energy difference²⁸ between the wurtzite and rocksalt phases of these ionic semiconductors is also so large that it is extremely difficult to stabilize the high pressure rocksalt phase under ambient conditions even with the best epitaxial stabilization techniques.^{29,30}

Given such constraints and with the motivation to understand the microstructural and morphological evolution during rocksalt-to-wurtzite structural phase transition that are essential for our pursuit of developing high temperature energy conversion materials and devices, we have performed an in-depth and detailed analysis of the $\text{Al}_x\text{Sc}_{1-x}\text{N}$ phase transition by capturing an intermediate mixed phase state having both stable wurtzite and metastable rocksalt phases in an aluminum scandium nitride ($\text{Al}_x\text{Sc}_{1-x}\text{N}$) thin film alloy grown on a 20 nm TiN seed layer deposited onto a (001) MgO substrate. The microstructural details studied by high-resolution electron microscopy reveal fascinating details that are likely to apply beyond the $\text{Al}_x\text{Sc}_{1-x}\text{N}$ system.

AlN (like other III–V nitrides) can be stabilized in the rocksalt crystal structure with an extremely small critical thickness of 2–3 nm inside a rocksalt TiN/AlN multilayer.³¹ Further increase in AlN thickness results in the nucleation of its wurtzite phase on the metastable rocksalt underlayer. TEM evidence also suggests that the rocksalt underlayer transitions to the wurtzite phase during growth. A critical thickness of about 2–3 nm is too small for any detailed

microscopic and crystallographic analyses that would microstructurally resemble the bulk or thin-film phase transition of these nitrides under pressure. Therefore, we have grown $\text{Al}_x\text{Sc}_{1-x}\text{N}$ alloys by dc-magnetron co-sputtering inside a high vacuum chamber on a 20 nm TiN seed layer on a (001) MgO substrate, adjusting x to yield rocksalt $\text{Al}_x\text{Sc}_{1-x}\text{N}$ films with large critical thicknesses (in excess of 200 nm) at high AlN mole fractions ($x < 0.82$).^{5,13} Moreover, $\text{Al}_x\text{Sc}_{1-x}\text{N}$ films with $0.62 < x < 0.82$ can be grown in the metastable rocksalt form with a 20 nm TiN seed layer. The seed layer offers a more compatible substrate for the film due to epitaxial stabilization and the compatible bond polarization of TiN compared to MgO.^{5–13} Since the critical thickness of the rocksalt-to-wurtzite phase transition is relatively large, for this study, we have grown a mixed-phase alloy with a composition ($\text{Al}_{0.84}\text{Sc}_{0.16}\text{N}$) slightly beyond the range for which the metastable rocksalt phase can be stabilized in 120 nm-thick films. The $\text{Al}_{0.84}\text{Sc}_{0.16}\text{N}$ alloy films described here are 120 nm in thickness and are grown on a 20 nm TiN seed layer, as described, on an (001) oriented MgO substrate. Details of the growth process are presented in the [supplementary material](#) section.

X-ray diffraction spectra from the 120 nm $\text{Al}_{0.84}\text{Sc}_{0.16}\text{N}$ /20 nm TiN/MgO thin film (see Fig. 1(a)) confirm the mixed-phase alloy sample with 002 $\text{Al}_{0.84}\text{Sc}_{0.16}\text{N}$ rocksalt, 0001 $\text{Al}_{0.84}\text{Sc}_{0.16}\text{N}$ wurtzite, 002 TiN and 002 MgO diffraction peaks clearly distinguishable in the spectrum. The 002 rocksalt $\text{Al}_{0.84}\text{Sc}_{0.16}\text{N}$ peak corresponds to an out-of-plane lattice constant (c) of 4.12 Å, which is very close to that of the

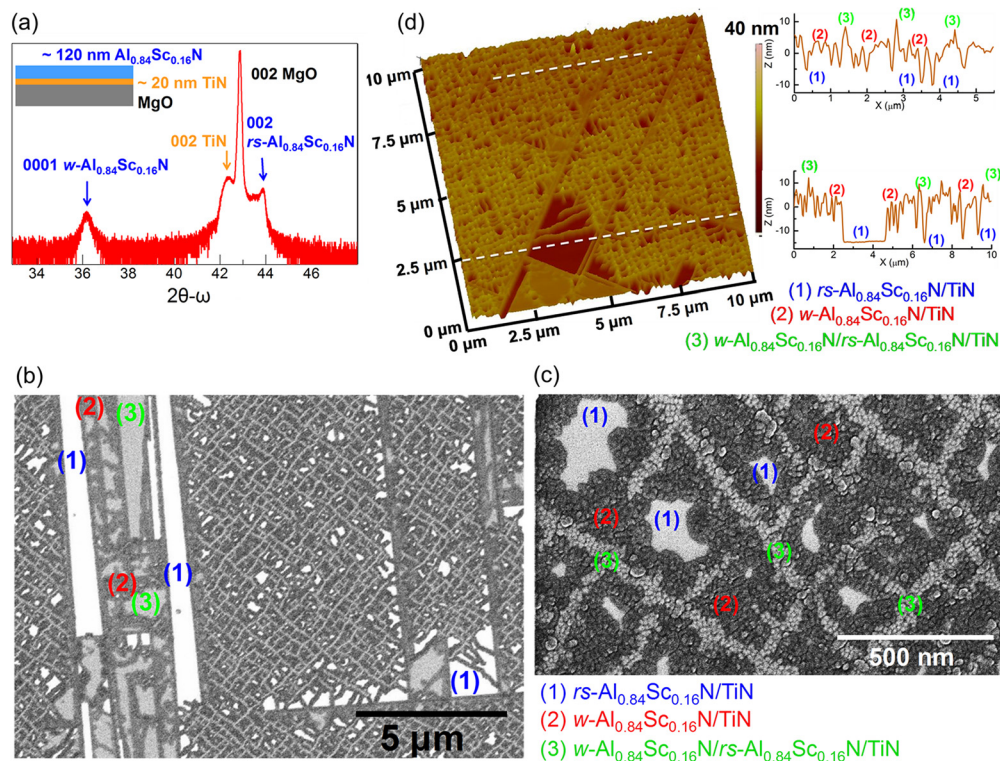


FIG. 1. (a) Symmetric 2θ - ω X-ray diffraction spectra of $\text{Al}_{0.84}\text{Sc}_{0.16}\text{N}$ film grown on (001) MgO substrate. 002 rocksalt- $\text{Al}_{0.84}\text{Sc}_{0.16}\text{N}$, 0002 wurtzite- $\text{Al}_{0.84}\text{Sc}_{0.16}\text{N}$, 002 TiN and 002 MgO diffraction peaks are clearly visible in the spectrum. (b) Plan-view SEM image of the mixed phase $\text{Al}_{0.84}\text{Sc}_{0.16}\text{N}$ sample that shows various microstructures and their morphology. The dark patches are wurtzite- $\text{Al}_{0.84}\text{Sc}_{0.16}\text{N}$ grown directly on (001)TiN/(001)MgO surface (we cannot exclude the presence of a thin rocksalt- $\text{Al}_{0.84}\text{Sc}_{0.16}\text{N}$ interlayer), the gray lines are also wurtzite- $\text{Al}_{0.84}\text{Sc}_{0.16}\text{N}$ but have grown on top of rocksalt- $\text{Al}_{0.84}\text{Sc}_{0.16}\text{N}$. The bright white pyramidal features are rocksalt- $\text{Al}_{0.84}\text{Sc}_{0.16}\text{N}$ that is exposed on the sample surface. (c) High-resolution SEM image of the $\text{Al}_{0.84}\text{Sc}_{0.16}\text{N}$ film that shows that the wurtzite- $\text{Al}_{0.84}\text{Sc}_{0.16}\text{N}$ regions are composed of small grains with grain size that varies from 10 to 20 nm. (d) AFM image of the sample that shows that the dark wurtzite- $\text{Al}_{0.84}\text{Sc}_{0.16}\text{N}$ grains are 10 to 15 nm larger in thickness compared to the light $\text{Al}_{0.84}\text{Sc}_{0.16}\text{N}$ seen in SEM images.

metastable rocksalt AlN's lattice constant³¹ of 4.08 Å. The 0001 wurtzite diffraction peak represents domains with *c*-axis wurtzite Al_{0.84}Sc_{0.16}N crystal growth with an out-of-plane lattice constant (*c*) of 4.94 Å, which is also very close to the *c*-axis lattice constant³¹ of stable wurtzite AlN (5.00 Å). The 002 TiN and 002 MgO diffraction peaks correspond to lattice constants of 4.23 Å, and 4.21 Å, respectively, consistent with the literature values.^{5,13,32}

Plan-view SEM images were obtained to understand the planar morphology of the crystal phases and microstructures in secondary electron emission mode. The SEM images (in Figs. 1(b) and 1(c)) show a surface morphology with several differing-contrast regions. The images show dark rectangular crystal patches of 100–400 nm in length and width, which are aligned vertically along the [100] directions of the (001)TiN/(001)MgO substrate. These dark patches are separated by grayish linear features that cut across them in the perpendicular in-plane directions. Fig. 1(c) shows that the dark regions in the SEM images consist of small dark-contrast grains with a diameter of 20–30 nm. The grayish lines that cut through the patches are also composed of similar small grains. Our TEM analysis described below reveals that these small grains have the wurtzite crystal structure with image contrast depending on whether these grains (dark) grow directly from the (001)TiN/(001)MgO surface (dark) or on top of a thin rocksalt-Al_{0.84}Sc_{0.16}N film (also dark) or on top of thicker rocksalt-Al_{0.84}Sc_{0.16}N islands (grayish). Fig. 1(c) also shows some solid light-contrast crystals in the center of some of the rectangular regions that have a much larger crystal size. We shall see later that these light-contrast crystals are rocksalt-Al_{0.84}Sc_{0.16}N that grow directly from the (001)TiN/(001)MgO surface and reach the top of the sample surface. The central portion of Fig. 1(b) consists of larger strips of these two types of crystal morphologies.

The electron contrast among different grains in the SEM image can be explained in terms of the secondary electron emission from these grains. The electron emission is mostly limited to the top few tens of nanometers of the surface.³³ Rocksalt and wurtzite grains in the Al_{0.84}Sc_{0.16}N film have similar compositions (as we will see later from the high-resolution transmission electron microscopy - energy-dispersive x-ray spectroscopy (HRTEM-EDX) analysis), therefore the penetration depth of the primary electrons is expected to be similar, differing by a factor comparable to the molar volume ratio. The secondary electrons that are generated, however, will have significantly different characteristics. In the case of rocksalt-Al_{0.84}Sc_{0.16}N/TiN/MgO, the secondary electron flux is expected to be greater due to relatively high conductivity and carrier concentrations (in the range of 10¹⁹–10²⁰ cm⁻³) arising from nitrogen vacancies and oxygen impurities (see Ref. 34). Wurtzite-Al_{0.84}Sc_{0.16}N is insulating. Moreover, the high resistivity of the wurtzite-Al_{0.84}Sc_{0.16}N would result in the build up of static charge on the surface that would repel the incoming primary electrons and reduce the subsequent generation of secondary electrons. From these considerations, the rocksalt-Al_{0.84}Sc_{0.16}N/TiN/MgO would be expected to have the brightest contrast, followed by wurtzite-Al_{0.84}Sc_{0.16}N/rocksalt-Al_{0.84}Sc_{0.16}N/TiN/MgO and wurtzite-Al_{0.84}Sc_{0.16}N/TiN/MgO, which is consistent with the experimental SEM images.

The AFM micrograph in Fig. 1(d) shows clearly the *z*-height variations among different microstructures present in the SEM image. The light-contrast regions (rocksalt-Al_{0.84}Sc_{0.16}N) are 10–12 nm lower in height in comparison to the dark grains (wurtzite-Al_{0.84}Sc_{0.16}N). The grayish grains that separate the dark rectangular patches are 6–8 nm lower in height in comparison to the dark grains, since they grow on top of the rocksalt-Al_{0.84}Sc_{0.16}N. The phase boundaries manifest quite clearly in the AFM images.

To identify the crystal structures and microstructural relationships, cross-sectional HRTEM and TEM-EDX analyses were performed. Details of the TEM sample preparation and microscopy techniques are presented in the [supplementary material](#) section of the manuscript. The TEM sample was prepared from a section of the sample that resembles a horizontal cross-section of Fig. 1(b) and included the full range of observed microstructures (see Fig. S1 in the [supplementary material](#)). The microscopy analyses, seen in Fig. 2, show pyramidal rocksalt-Al_{0.84}Sc_{0.16}N crystals (seen as dark triangular regions in Fig. 2(a)) separated by the wurtzite-Al_{0.84}Sc_{0.16}N matrix (seen as bright regions). The base of these rocksalt-Al_{0.84}Sc_{0.16}N pyramids originates from the (002) TiN buffer layer, and they vary in their lateral dimensions from 50 to 150 nm. Most of the rocksalt pyramids are separated by approximately 50 to 100 nm, and in some cases two pyramids are seen to be merging with one another. Though most of the rocksalt-Al_{0.84}Sc_{0.16}N pyramids are embedded within the film with wurtzite grains on top (appearing gray in contrast in the SEM images of Figs. 2(a) and 2(c)), there are some pyramids that reach the top of the sample surface (corresponding to bright white patches in SEM images). The boundaries between the rocksalt and wurtzite phase are sharp, as evidenced by the high-resolution image in Fig. 2(b). The rocksalt 20 nm TiN seed layer appears dark in the HRTEM image. Hexagonal lattice fringes are clearly visible in the upper regions of Fig. 2(b), which correspond to the wurtzite structure. Similarly, cubic lattice fringes representing rocksalt-Al_{0.84}Sc_{0.16}N are seen in the lower portion of the figure.

Fig. 2(a) also shows that the wurtzite-Al_{0.84}Sc_{0.16}N growth fronts move faster compared to the rocksalt growth

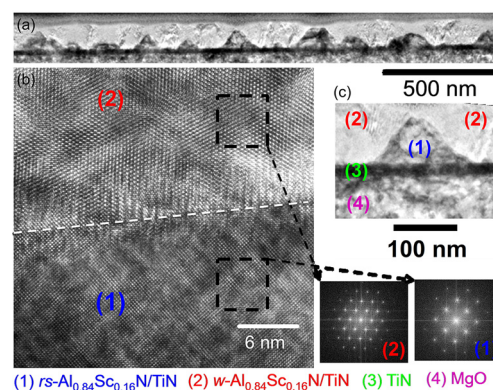


FIG. 2. (a) Low magnification cross-sectional HRTEM image of the mixed phase Al_{0.84}Sc_{0.16}N film. The pyramids are rocksalt-Al_{0.84}Sc_{0.16}N with their peaks mostly terminating inside the film. Wurtzite-Al_{0.84}Sc_{0.16}N grains separate the pyramids. (b) HRTEM image of rocksalt-wurtzite phase boundary. FFTs taken from each phase are also presented. (c) High resolution HRTEM image of a pyramid is presented and different materials and crystal phases are identified.

front due to the larger volume of the wurtzite unit cell in comparison to the rocksalt unit cell. The volume of a wurtzite- $\text{Al}_{0.84}\text{Sc}_{0.16}\text{N}$ unit cell is about 24% larger than a rocksalt- $\text{Al}_{0.84}\text{Sc}_{0.16}\text{N}$ unit cell. As a result, the wurtzite- $\text{Al}_{0.84}\text{Sc}_{0.16}\text{N}$ regions are about 20% thicker compared to the rocksalt- $\text{Al}_{0.84}\text{Sc}_{0.16}\text{N}$ regions, as demonstrated in Fig. 2(a), where it can be seen that the film is thinner above the rocksalt pyramidal peaks. The high magnification TEM image Fig. 2(b) shows clear and distinct lattice fringes from both the rocksalt and wurtzite phases. A Fast Fourier Transform (FFT) from the wurtzite grain shows a hexagonal diffraction pattern, with the wurtzite grains having their c -axis parallel to the in-plane $[100]$ direction of the TiN/MgO substrate. In fact, most of the wurtzite grains that are present in the film have their c -axes oriented parallel to the substrate, which the XRD analysis presented earlier (Fig. 1(a)) could not capture. Because of the higher growth rate of the wurtzite grains, they also have higher z -height in the AFM images. Rocksalt- $\text{Al}_{0.84}\text{Sc}_{0.16}\text{N}$ pyramid tops that reach the surface appear bright in the SEM image.

The TEM-EDX analyses suggest there was no significant compositional difference between the rocksalt- $\text{Al}_x\text{Sc}_{1-x}\text{N}$ and wurtzite- $\text{Al}_x\text{Sc}_{1-x}\text{N}$ phases as seen in the regions inside and outside of the pyramidal structures, respectively. Quantitative estimates from the EDX analysis also suggest that the composition of the phases remains unchanged throughout different regions of the film (about $2\ \mu\text{m}^2$ studied in the TEM analysis). The absence of compositional variation indicates that the phase transition is triggered by defect accumulation at the growth front, rather than interdiffusion or surface diffusion during or after the growth process.

HRTEM studies also reveal intricate microstructural relationships between the different phases. Although the wurtzite- $\text{Al}_{0.84}\text{Sc}_{0.16}\text{N}$ grains are polycrystalline with very small crystal sizes, they are not random in orientation. They often exhibit twin relationships to each other as seen in Fig. 3. Two wurtzite- $\text{Al}_{0.84}\text{Sc}_{0.16}\text{N}$ grains are seen that are rotated with respect to each other about their common $[0001]$ axis. The epitaxial

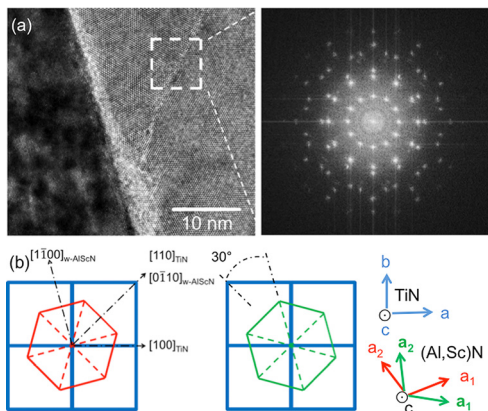


FIG. 3. (a) High resolution TEM image of the mixed phase $\text{Al}_{0.84}\text{Sc}_{0.16}\text{N}$ film that shows two wurtzite- $\text{Al}_{0.84}\text{Sc}_{0.16}\text{N}$ grains rotated by 30° with respect to each other. The bottom 20 nm TiN seed layers are clearly visible, as well as some $\text{Al}_{0.84}\text{Sc}_{0.16}\text{N}$ regions. FFT taken from a highlighted region that shows 12 diffraction spots originating from two grains rotated by 30° with respect to the c -axis of the wurtzite phase. (b) Epitaxial relationships of the wurtzite twins with TiN are presented. The two twin variants are rotated 30° with respect to each other as shown.

relationships between the two wurtzite- $\text{Al}_{0.84}\text{Sc}_{0.16}\text{N}$ and the rs -TiN (which may be covered with a pseudomorphic rs - $\text{Al}_{0.84}\text{Sc}_{0.16}\text{N}$ thin film) are $(0001)[0\bar{1}10]$ $\text{Al}_{0.84}\text{Sc}_{0.16}\text{N}$ || $(001)[110]$ TiN and $(0001)[1\bar{1}00]$ $\text{Al}_{0.84}\text{Sc}_{0.16}\text{N}$ || $(001)[110]$ TiN. In the FFT (Fig. 3(b)) collected from a square region comprising the two variants, twelve diffraction spots that are 30° apart are seen. They are due to the presence of the two different wurtzite- $\text{Al}_{0.84}\text{Sc}_{0.16}\text{N}$ grain orientations rotated 30° with respect to each other about the common $[0001]$ axis. The twelve diffraction spots originate from wurtzite- $\text{Al}_{0.84}\text{Sc}_{0.16}\text{N}$ grains whose basal planes are perpendicular to the substrate surface.

The development of the complex microstructure of these films can be rationalized based on straightforward energetic considerations. Since the rocksalt- $\text{Al}_{0.84}\text{Sc}_{0.16}\text{N}[001]$ and TiN $[001]$ are isostructural and nearly lattice-matched, the excess interface free energy is expected to be very low as is the strain energy stored in the lattice-coherent film/substrate couple. Although the stable $\text{Al}_{0.84}\text{Sc}_{0.16}\text{N}$ phase in the bulk is wurtzite, the higher excess interface free energy of the wurtzite/rocksalt-TiN interface favors rocksalt- $\text{Al}_{0.84}\text{Sc}_{0.16}\text{N}$ growth in a planar film from a free energy standpoint. As the rocksalt film thickens, kinetic barriers to the nucleation of the wurtzite phase will allow pseudomorphic growth beyond the maximum (“critical”) thickness for which the rocksalt film has a lower free energy. Note that a sample with 5 nm $\text{Al}_{0.84}\text{Sc}_{0.16}\text{N}/\text{TiN}/\text{MgO}$ (not shown) remained planar and pseudomorphic with no signs of wurtzite.

As the rocksalt film thickens beyond the critical thickness defined above, the accumulation of strain and lattice defects increase the driving force and lower the barrier for nucleation of wurtzite- $\text{Al}_{0.84}\text{Sc}_{0.16}\text{N}$ as in the case of CrN/TiN superlattices.³⁵ As the wurtzite phase nucleates, it does not do so randomly from a crystallographic standpoint. Our cross-sectional HRTEM and diffraction data reveals a preferential orientation relationship for the wurtzite grains that nucleate directly on a rocksalt surface. The 30° rotation boundaries between wurtzite grains with their c -axes parallel to $\langle 100 \rangle$ directions in substrate surface produce four crystallographic variants.

Examining Figure 2, it is evident that a wurtzite- $\text{Al}_{0.84}\text{Sc}_{0.16}\text{N}$ grain has impinged with a rocksalt- $\text{Al}_{0.84}\text{Sc}_{0.16}\text{N}$ grain to form an interface that is inclined to the substrate surface. That interface contains the parallel w - $[0001]$ and rs - $[100]$ directions. The interface plane can be defined as close to rs - $(0\bar{1}1)$ which is parallel to w - $(2\bar{1}\bar{1}0)$. Figure 4(a) illustrates this orientation relationship in real space. Both crystal structures present a rectangular lattice on this plane whose unit cells differ in area by 11.7%, and consist of 2 nitrogen anions and 2 metal cations.

Ab-initio simulations by Limpijumngong and Lambrecht²⁸ and Saitta and Decremps,²⁶ and metadynamics analysis performed recently by Duan *et al.*³⁶ have suggested that the phase transition in AlN should involve a hexagonal intermediate state transformation path driven by homogeneous orthorhombic shear strain. The transition path is expected to be a two-step process according to the modeling analysis. In the first-step, the (c/a) ratio should decrease leading to a hexagonal intermediate state, and in the second the hexagonal angles should open with the atoms at the center of the triangles moving horizontally at the center of the square, thus leading to a

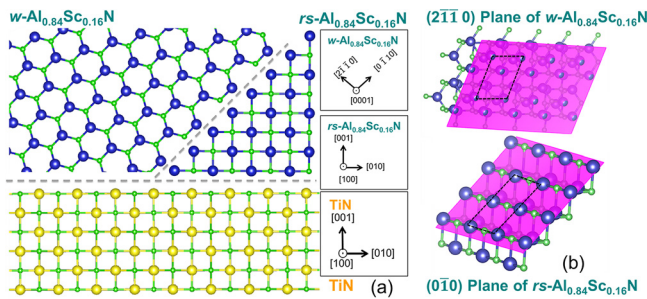


FIG. 4. (a) Epitaxial relationship between the rocksalt- $\text{Al}_{0.84}\text{Sc}_{0.16}\text{N}$ and wurtzite- $\text{Al}_{0.84}\text{Sc}_{0.16}\text{N}$ phases seen in Fig. 2(b) is presented. The rocksalt and wurtzite grains impinge with the interface inclined to the substrate surface. The interface plane is close to $rs\text{-}(0\bar{1}1)$ which is parallel to $w\text{-}(2\bar{1}0)$. (b) The $w\text{-}(2\bar{1}0)$ and $rs\text{-}(0\bar{1}1)$ planes are shown with their unit cells and distribution of atoms on these planes. The unit cell area differs by 11.7% and is composed of 4 atoms in each phase at the interface.

rocksalt crystal. It is also expected that the relative crystallographic orientations between the wurtzite and rocksalt phase should follow a simple relation $w\text{-}(0001) \parallel rs\text{-}(001)$.

Crystallography and epitaxial details observed in the present study confirm the $w\text{-}(0001) \parallel rs\text{-}(001)$ relationship. In addition, approximate conservation of in-plane unit cell area, number, and distribution of atoms on the plane and polarity have ensured that $w\text{-}(2\bar{1}0) \parallel rs\text{-}(0\bar{1}1)$. Therefore, the microstructural and epitaxial details observed in this study are consistent with the hexagonal intermediate state transition mechanism driven by shear strain. This is the first direct experimental support for this transition mechanism.

Synchrotron XRD evidence for these same variants was reported in a previous publication (Ref. 14) involving TiN/rocksalt- $\text{Al}_{0.72}\text{Sc}_{0.28}\text{N}$ superlattices subjected to high temperature annealing during which the metastable rocksalt phase transformed to wurtzite. The films in the present study were deposited at 750°C . The films in the annealing study were subjected to higher temperatures, between 950°C and 1050°C . Although we cannot rule out that some deposited rocksalt- $\text{Al}_{0.84}\text{Sc}_{0.16}\text{N}$ transformed to the wurtzite phase during subsequent deposition at 750°C , previous annealing studies of similar films have shown no evidence of this phase transition at temperatures this low.

In conclusion, we have investigated the microstructural development in a model system for understanding the rocksalt-to-wurtzite phase transformation. The ability to tune the relative free energies of the rocksalt and wurtzite phases in the $\text{Al}_x\text{Sc}_{1-x}\text{N}$ system by adjusting the AlN mole fraction allows one to capture what is essentially a thin-film snapshot of the transformation in progress. These data and mechanisms are important in determining the full range of thin-film growth conditions, thicknesses, and compositions that will yield rocksalt films and metal/semiconductor superlattices of high crystal quality and adequate thermal stability for device applications. Furthermore, the crystallographic features of the transformation from rocksalt to wurtzite phases in this system are expected to carry over to other material systems that exhibit both of these phases.

See the [supplementary material](#) for details about thin-film growth method, X-ray diffraction, and HRTEM details.

B.S. and T.D.S. acknowledge financial support from the National Science Foundation and U.S. Department of Energy (Award No. CBET-1048616). E.A.S. acknowledges support from the Center for Functional Nanomaterials, Brookhaven National Laboratory, which is supported by the U.S. Department of Energy, Office of Basic Energy Sciences, under Contract No. DE-AC02-98CH10886. The authors declare no competing financial interests.

- ¹D. Vashaev and A. Shakouri, *Phys. Rev. Lett.* **92**, 106103 (2004).
- ²B. Saha, A. Shakouri, and T. D. Sands, "Metal/semiconductor superlattices: Development of an elusive heterostructure," (submitted).
- ³V. Rawat, Y. Koh, D. Cahill, and T. Sands, *J. Appl. Phys.* **105**, 024909 (2009).
- ⁴B. Saha, Y. R. Koh, J. Comparan, S. Sadasivam, J. L. Schroeder, J. Birch, T. Fisher, A. Shakouri, and T. D. Sands, *Phys. Rev. B* **93**, 045311 (2016).
- ⁵B. Saha, G. V. Naik, S. M. Saber, C. Akatay, E. A. Stach, V. M. Shalaev, A. Boltasheva, and T. D. Sands, *Phys. Rev. B* **90**, 125420 (2014).
- ⁶G. V. Naik, B. Saha, J. Liu, S. M. Saber, E. A. Stach, J. M. K. Irudayaraj, T. D. Sands, V. M. Shalaev, and A. Boltasheva, *Proc. Natl. Acad. Sci.* **111**, 7546 (2014).
- ⁷J. P. Harbison, T. Sands, N. Tabatabaie, W. K. Chan, L. T. Florez, and V. G. Keramidis, *Appl. Phys. Lett.* **53**, 1717 (1988).
- ⁸U. Guler, A. Boltasheva, and V. M. Shalaev, *Science* **344**, 263 (2014).
- ⁹U. Guler, A. Kildishev, A. Boltasheva, and V. M. Shalaev, *Faraday Discuss.* **178**, 71 (2015).
- ¹⁰G. V. Naik, V. M. Shalaev, and A. Boltasheva, *Adv. Mater.* **25**, 3264 (2013).
- ¹¹S. Adachi, *Properties of Semiconductor Alloys: Group-IV, III-V and II-VI Semiconductors* (John Wiley & Sons, Chichester, 2009).
- ¹²J. Wu, W. Walukiewicz, K. M. Yu, J. W. Ager III, E. E. Haller, H. Lu, and W. J. Schaff, *Appl. Phys. Lett.* **80**, 4741 (2002).
- ¹³B. Saha, S. Saber, G. V. Naik, A. Boltasheva, E. Stach, E. P. Kvam, and T. D. Sands, *Phys. Status Solidi B* **252**, 251 (2015).
- ¹⁴J. L. Schroeder, B. Saha, M. Garbrecht, N. Schell, T. D. Sands, and J. Birch, *J. Mater. Sci.* **50**(8), 3200–3206 (2015).
- ¹⁵M. Garbrecht, B. Saha, J. L. Schroeder, L. Hultman, and T. D. Sands, "Dislocation pipe diffusion in nitride superlattices observed in lattice resolved microscopy," (submitted).
- ¹⁶M. Ueno, A. Onodera, O. Shimomura, and K. Takemura, *Phys. Rev. B* **45**, 10123 (1992).
- ¹⁷Q. Xia, H. Xia, and A. L. Ruoff, *J. Appl. Phys.* **73**, 8198 (1993).
- ¹⁸H. Xia, Q. Xia, and A. L. Ruoff, *Phys. Rev. B* **47**, 12925 (1993).
- ¹⁹S. Hull and D. A. Keen, *High Pressure Res.* **14**, 121 (1995).
- ²⁰S. Hull and D. A. Keen, *Phys. Rev. B* **50**, 5868 (1994).
- ²¹A. Seko, F. Oba, A. Kuwabara, and I. Tanaka, *Phys. Rev. B* **72**, 024107 (2005).
- ²²S. Desgreniers, *Phys. Rev. B* **58**, 14102 (1998).
- ²³Z. Wang, K. Tait, Y. Zhao, D. Schiferl, C. Zha, H. Uchida, and R. Downs, *J. Phys. Chem. B* **108**, 11506 (2004).
- ²⁴P. Perlin, C. Jaubertie-Carillon, J. P. Itie, A. S. Miguel, I. Grzegory, and A. Polian, *Phys. Rev. B* **45**, 83 (1992).
- ²⁵F. J. Manjon, D. Errandonea, N. Garro, A. H. Romero, J. Serrano, and M. Kuball, *Phys. Status Solidi B* **244**, 42 (2007).
- ²⁶A. M. Saitta and F. Decremps, *Phys. Rev. B* **70**, 035214 (2004).
- ²⁷I. Gorczyca, N. E. Christensen, P. Perlin, I. Grzegory, J. Jun, and M. Bockowski, *Solid State Commun.* **79**, 1033 (1991).
- ²⁸S. Limpitjumnong and W. R. L. Lambrecht, *Phys. Rev. Lett.* **86**, 91 (2001).
- ²⁹J. Serrano, A. Rubio, E. Hernández, A. Muñoz, and A. Mujica, *Phys. Rev. B* **62**, 16612 (2000).
- ³⁰N. E. Christensen and I. Gorczyca, *Phys. Rev. B* **47**, 4307 (1993).
- ³¹A. Madan, I. W. Kim, S. C. Cheng, P. Yashar, V. P. Dravid, and S. A. Barnett, *Phys. Rev. Lett.* **78**, 1743 (1997).
- ³²B. L. Thiel and M. Toth, *J. Appl. Phys.* **97**, 051101 (2005).
- ³³B. Saha, S. K. Lawrence, J. L. Schroeder, J. Birch, D. F. Bahr, and T. D. Sands, *Appl. Phys. Lett.* **105**, 151904 (2014).
- ³⁴P. V. Burmistrova, J. Maassen, T. Favaloro, B. Saha, S. Salamat, Y. R. Koh, M. S. Lundstrom, A. Shakouri, and T. D. Sands, *J. Appl. Phys.* **113**, 153704 (2013).
- ³⁵P. Yashar, X. Chu, S. A. Barnett, J. Rechner, Y. Y. Wang, M. S. Wong, and W. D. Sproul, *Appl. Phys. Lett.* **72**, 987 (1998).
- ³⁶Y. Duan, L. Qin, and H. Liu, *J. Phys.: Condens. Matter* **28**, 205403 (2016).